International Journal of Heat and Mass Transfer 146 (2020) 118830

Contents lists available at ScienceDirect

International Journal of Heat and Mass Transfer

journal homepage: www.elsevier.com/locate/ijhmt

Heat transfer and melt dynamics of millimetric ice particles impacting a heated water bath

Katherine Baskin [a], Katharine M. Flores [a,b], Patricia B. Weisensee [a,b,*]

[a] Department of Mechanical Engineering & Materials Science, Washington University in St. Louis, USA
[b] Institute of Materials Science and Engineering, Washington University in St. Louis, USA

ARTICLE INFO

Article history:
Received 22 May 2019
Received in revised form 29 August 2019
Accepted 1 October 2019

Keywords:
Particle impact
Nusselt correlation
Phase change
Melting
Heat transfer
Additive manufacturing

ABSTRACT

In metallic additive manufacturing using direct energy deposition, particles and melt pool undergo complex interactions, including particle impact, penetration, and melting. The spatio-temporal evolution of these processes dictates the solidified material microstructure and final workpiece quality. However, due to the opaqueness of metallic melt pools, in-situ visualization is nearly impossible. To model this system, we use high-speed imaging to investigate the heat transfer and melting dynamics of spherical ice particles ($D \approx 2$ mm) impacting heated water baths of varying temperatures (23–70 °C) with velocities ranging from 0.8 to 2.1 m/s. To visualize the outflow of molten ice, representative of mixing and material homogeneity, the particles were colored with food dye. We show that after impact, molten liquid forms an annular plume travelling downwards in the bath, until hitting the bottom of the enclosure and expanding radially. Due to positive buoyancy forces, unmolten ice particles rise to the top of the water bath, where they fully melt. As temperatures increase, we observe random particle movement, indicating the presence of convective currents. Through video analysis, we examine the relationships between bath temperature, impact velocity, and heat transfer. As expected, increasing the bath temperature decreases the total melt time of the ice particle. Interestingly, the impact velocity has only a minor effect on the melting time. Using non-dimensional analysis, we derive an expression for the correlation between Nusselt and Stefan numbers. Insights from this work can be used to match characteristic time scales during additive manufacturing to tailor material properties.

1. Introduction

Additive manufacturing (AM) comprises a fast evolving and revolutionary set of technologies for manufacturing components with complex shapes, typically for applications requiring low-to-moderate part counts. Evolving from the ubiquitous "3D printing" technologies used to construct model or prototype parts from polymeric fibers, industrial-scale methods now exist that can construct high-quality, production-scale parts from metals and ceramics. A subset of AM methods, direct energy deposition (DED), uses a concentrated energy source such as a laser or electron beam to create a melt pool on the surface of a workpiece. A stream of solid powder particles is fed into the melt pool, which then quenches rapidly as the energy source and powder stream raster across the surface of the workpiece to create a newly deposited layer of material. Processing parameters, including the power of the energy source, its travel speed relative to the workpiece, and the composition and flow rate of the powder, can be adjusted to control the local thermal conditions during deposition and thereby control the local microstructure and composition of the final part [1–3].

While the highly localized nature of the DED process provides the opportunity to optimize the material microstructure and composition as a function of position within the part, numerous questions remain about the physical processes occurring within the melt pool during deposition. These influence both the evolution of the microstructure and the formation of defects, including voids or undesirable compositional variations associated with incomplete melting or mixing of the powder in the melt pool [4,5]. Unfortunately, in-situ characterization of the melt pool and powder particle dynamics remains a challenge due to the inaccessibility and opaqueness of the melt pool [6,7].

In the present work, we construct a model system to investigate the particle-melt pool interactions during impact and particle melting. Quasi-spherical ice particles and water are used as analogs for the powder and melt pool, respectively, and are imaged using high-speed cameras during particle impact and subsequent

* Corresponding author at: Department of Mechanical Engineering & Materials Science, Washington University in St. Louis, USA.
E-mail address: p.weisensee@wustl.edu (P.B. Weisensee).

https://doi.org/10.1016/j.ijheatmasstransfer.2019.118830
0017-9310/

melting into the liquid medium. Indeed, water-ice analogies have been used in the past to study keyhole and bubble formation during aluminum welding [8]. To facilitate the comparison between a DED process (using stainless steel) and the model system, we match key dimensionless parameters as closely as possible, as summarized in Table 1. In particular, a good match of Weber numbers, representing inertial *vs.* surface tension forces, is expected to lead to similar impact and penetration dynamics. A good match of Stefan numbers, comparing sensible heat and latent heat of the particle, represents comparable heat transfer and melting dynamics. The latter is particularly important, given the relatively high superheat of the melt pool during DED (50–600 °C) compared to modest superheats during the present experiments (23–70 °C) [9,10]. Non-dimensionalizing experimental parameters and findings (*e.g.*, Nusselt number representing heat transfer rates) allow us to transfer results from the model system to typical DED processes. Insights from this study will enhance our understanding of the impact and phase change dynamics during DED and support the advancement of additive manufacturing processes.

Melting of spherical particles has been studied for both metals and ice under forced convective flow [15–18]. In these studies, heat transfer increases with flow rate and is highest at the leading and trailing edges of the spherical particles. A circulating wake forms behind the particles. Sphere and droplet impact into a quiescent surface is also documented, with notable features like bubble entrapment [19–21] and vortex generation [22]. Similarly, during droplet impact and coalescence in miscible liquids, vortex ring propagation and splashing are observed [22–28]. Past research has been limited to melting of spherical particles under constant flow rates or (isothermal) particle impact without phase change. With this investigation, we set out to observe the integrated relation between particle impact, melting, and the influence of temperature and impact velocity.

2. Experimental setup

To create approximately spherical ice particles, de-ionized (DI) water was first boiled for de-gassing and dyed with blue food coloring. Using a 33 gauge needle, equal-sized droplets ($D \approx 2$ mm) were deposited on a petri dish coated with *Glaco Mirror Coat* (liquid water static contact angle of 165° ± 3° with negligible hysteresis). The droplets were then placed in a freezer (−20 °C) to form quasi-spherical ice particles of consistent size and shape. Upon freezing, the contact angle decreased slightly to 135° ± 5°, leading to ice particles with a spherical cap shape, as shown in the inset of Fig. 1, with $D_{x,y} \approx 2$ mm and $D_z \approx 1.8$ mm. These ice particles then impacted onto a DI water bath. Despite short handling times, a thin liquid film might have formed on the particle surface prior to impact due to thermal conduction to tweezers and natural and forced convection during free fall. Water was selected as bath fluid for its transparency and miscibility with the ice particles. The water was contained in a custom-built square borosilicate glass tank to avoid optical distortions. The bath was illuminated with a white backlight (Metaphase 3.5'' x 6'' backlight LED) for optimal video quality. A Photron Fastcam Mini AX200 high-speed (HS) camera with a Canon 1-5× 65 mm macro lens (1× setting) at a resolution of 27.5 μm/pixel was used to record ice impact and melting dynamics. The camera was positioned on a tripod parallel to the floor and focused on the center of the water bath as shown in Fig. 1. High acquisition rates at 10,000–15,000 frames per second (fps) were used to record the moment of impact. Lower frame rates (60–250 fps) were used to record the entire duration of the ice particle melt. At select experimental settings, an Edgertronic SC1 color high-speed camera with a Nikon 105 mm lens at a resolution of 22.3 μm/pix recorded the impact and melting dynamics in top-view to complement side-view information obtained with the Photron HS camera.

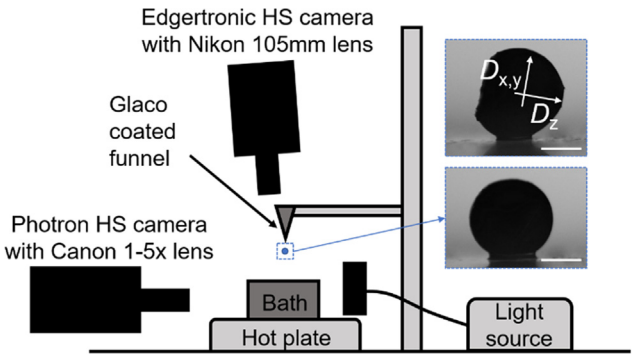

Fig. 1. Schematic of the experimental setup. Insets: Images of two perpendicular views of the ice particles, showing their deviation from a perfect spherical shape. Scale bar: 1 mm.

To ensure a consistent impact location and to minimize particle adhesion, the ice particles were directed using a Glaco-coated funnel. Ice spheres impacted from heights between 2 and 20 cm onto the water bath, resulting in impact velocities ranging from 0.8 to 2.1 m/s, as determined from additional high-speed video recordings just prior to impact. Velocities were averaged over several trials. For each impact height, the ice particles impacted baths of six different temperatures T_{bath} = 23, 30, 40, 50, 60 and 70 °C. To heat the bath, the glass tank was placed on a hotplate, and a thermocouple (Digi-Sense Type-K) measured the temperature approximately 3 mm beneath the liquid surface. Using particle image velocimetry (PIV), we found that thermal convective currents (*e.g.*, Rayleigh-Bénard convection) have only minor effects on particle dynamics during impact. For example, at T_{bath} = 60 °C the maximum measured liquid velocity is 0.01 m/s, resulting in a drag force two orders of magnitude smaller than buoyancy forces between the

Table 1
Comparison of typical DED parameters using stainless steel as working materials and corresponding test parameters in the model system (taken at 23–70 °C), along with relevant non-dimensional numbers defined as: *Re*: Reynolds number, *We*: Weber number, *Bo*: Bond number, *Ste*: Stefan number, *Ca*: Capillary number, where g is the gravitational constant [m/s^2], c_p is the specific heat capacity [kJ/kgK], h_{fs} is the enthalpy of fusion [kJ/kg], ρ is the density in [kg/m^3], and m^* is the specific mass ratio between the particle (p) and the liquid melt pool (l).

Parameter	DED	Model system	Non-dimensional number	DED	Model system
Particle size (D) [μm]	25–120 [11,12]	2000	$Re = \frac{\rho v D}{\mu}$	200–2000	3900–4650
Impact speed (v) [m/s]	6–12 [12]	0.8–2.1	$We = \frac{\rho v^2 D}{\gamma}$	3.5–70	20–122
Liquid surface tension γ [mN/m]	1700 [13]	64–72	$Bo = \frac{\rho g D^2}{\gamma}$	≪1	0.5–0.6
Liquid density ρ [kg/m^3]	7000 [13]	978–998	$Ste = \frac{c_p \Delta T_s}{h_{fs}}$	0.52–0.98	0.29–0.88
Liquid viscosity μ [mPa.s]	~5 [14]	0.4–0.9	$Ca = \frac{\mu v}{\gamma}$	0.02–0.04	0.01–0.03
Pool superheat ΔT_s [°C]	50–600 [9,10]	23–70	$m^* = \frac{\rho_p}{\rho_l}$	1.11	0.93

ice particles and the liquid bath. However, as will be shown in Section 4.1, thermal convective currents influence the dynamics of the particle after resurfacing and those of the melt. Three trials were conducted for each temperature-velocity combination.

3. Methods

To analyze particle melt dynamics and melting times, videos were processed using ImageJ. To isolate the ice particle from the background, we determined an intensity threshold for each recording and converted the individual frames to binary images. We assumed that this threshold remained constant throughout each video, given the constant lighting intensity for the duration of the recording. The black pixel count was then converted to an equivalent area A_{eq} using the known lens calibration (27.5 μm/pixel). The equivalent volume can be determined as $V_{eq} = \frac{4\pi}{3}(A_{eq}/\pi)^{3/2}$, and the equivalent diameter becomes $D_{eq} = \sqrt{4A_{eq}/\pi}$, assuming a spherical particle shape. This assumption has been previously used for melting metallic spherical particles [17]. Fig. 2a shows a typical evolution of the particle equivalent diameter for an ice particle impacting a water bath at 23 °C at an impact velocity of 2.1 m/s. The temporal evolution of the equivalent diameter can be used to determine the average heat transfer rate during melting. The time-dependent Nusselt number is [29]:

$$Nu = \frac{\rho_w h_{fs} D_{eq}}{2k_w \Delta T_s} \times \left|\frac{dD_{eq}}{dt}\right| \quad (1)$$

where ρ_w and k_w are density and thermal conductivity of the water bath, respectively, and $\Delta T_s = T_{bath} - T_{sat}$, where $T_{sat} = 0$ °C is the melting temperature of ice, and it was assumed that the dye has no effect on these properties. Thermo-physical properties of the bath were evaluated at the film temperature $T_{film} = (T_{sat} + T_{bath})/2$. As shown in Fig. 2b, the Nusselt number remains approximately constant during the melting process for times larger than a critical cut-off time, indicated by the vertical red line. Inconsistency in the Nusselt number towards the beginning of the melting process can be attributed to errors in ImageJ particle recognition due to bubble entrapment, and non-uniform melting dynamics. Hence, in the remainder of this work, we report the time-averaged Nusselt number above the cut-off time.

To estimate the error associated with assuming a spherical particle shape during image analysis, we divided the particle into horizontal and vertical 'pixel slices'. Each slice was rotated into a one-pixel thick cylinder, around the x or y axis. All cylinders were then added together to obtain a total volume. We found that throughout the melting, the error in volume between the spherical assumption and cylinder method was approximately 0.1–5%. This error is small enough that the spherical assumption is valid.

Error was also introduced when setting a threshold in ImageJ to distinguish the particle from background noise. Noise was most commonly seen along the particle edges and towards the bottom of the particle, where the intensity of the melt water was similar to that of the ice. In these cases, ImageJ was unable to distinguish between the melt plume and the un-molten particle, as shown in Fig. 3. The automatically determined resulting pixel area was approximately 3% higher than the actual particle area, as shown with the red color in Fig. 3c. Overall, the uncertainty associated with setting a constant intensity threshold ranged from 3% to 8%. The relative error was generally higher at later stages of melting due to a reduced particle size.

Combining the errors introduced by choosing a fixed intensity during image analysis and by assuming a spherical shape, we obtain an overall uncertainty for the determination of the equivalent diameter of 8.2%. Using the concept of error propagation, the uncertainty for the Nusselt number as stated in Eq. (1) is hence 16.4%, and is included – in addition to the standard deviation from multiple test runs – in the error bars of the Nu-Ste-correlation (Fig. 9).

4. Results and discussion

4.1. Visual observations: 3 stages of particle dynamics

Ice particles and molten liquid dynamics display three different stages after impact. As seen in Fig. 4a, the particle first penetrates and descends into the bath due to its downward facing momentum from the initial impact (stage 1). The particle slows down due to drag and positive buoyancy of ice with respect to liquid water as it descends. After reaching a maximum penetration depth, the particle rises and resurfaces (stage 2). After resurfacing, the particle maintains its vertical position just below the bath surface until it melts completely (stage 3). Interestingly, we observe particle rotation during impact and resurfacing, which in some cases leads to a deviation from the typical penetration profile of a particle, as shown in Fig. 4b. In some instances, the ice particle penetrates the bath but does not resurface; the particle is instead pulled downwards by convective currents. Other times, the particle barely

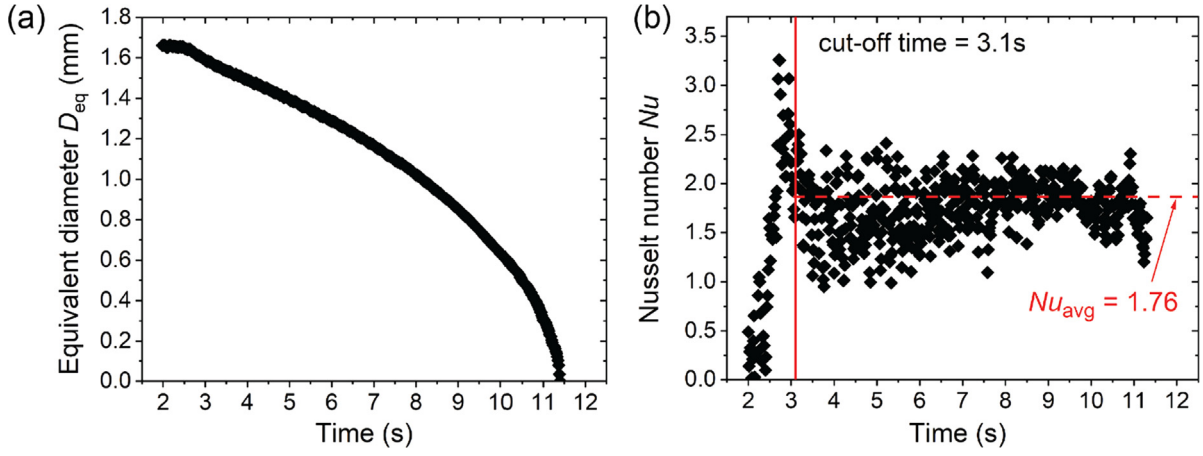

Fig. 2. (a) Time evolution of the equivalent particle diameter upon melting for an ice particle impacting a water bath (T_{bath} = 23 °C, v = 2.1 m/s). (b) Nusselt number as derived from (a) using Eq. (1), showing a cut-off time at 3.1 s. Above the cut-off, Nusselt numbers are approximately constant with time over the course of the total melt period with an average Nusselt number of 1.76.

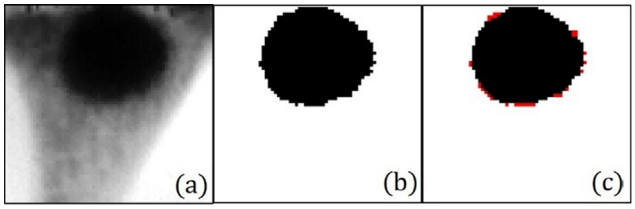

Fig. 3. (a) As-is image of an ice particle (dark gray/black pixels) with melt water (light gray/white pixels). (b) Processed image distinguishing the ice particle (black pixels) and melt/noise (white pixels). (c) Manually processed image distinguishing the ice particle (black pixels), melt/noise (white pixels), and error associated with the constant intensity threshold (red pixels). (For interpretation of the references to color in this figure legend, the reader is referred to the web version of this article.)

penetrates the surface before resurfacing; it appears to be pushed upwards. We attribute this variability in penetration dynamics to the generation of non-symmetric vortices around the particle [30], originating from the slightly asymmetric shape of the particles and the corresponding rotation of the particle during descent. Except for the lowest impact velocity, the existence, absence, or shape of the cavity does not seem to influence particle deceleration and penetration to a large extent. For a given impact velocity, initial particle deceleration is similar for multiple impact cases, and particles appear to come to a halt near the equilibrium (or average) penetration depth, as seen in the 40–60 ms time interval in Fig. 4b. At this moment particles which deviate from the common penetration profile depicted in Fig. 4a rotate and a non-symmetric vortex can be observed. Similar to observations made by Truscott *et al.* for rigid spheres [30], we believe that the forces generated by this vortex non-symmetry cause the droplet to sink further ($t > 60$ ms in Fig. 4b). Unfortunately, a detailed fluid dynamic analysis of the influence of particle shape and vortex generation is outside of the scope of this work. Overall, since we present in Section 4.4 the melting times and heat transfer rates for multiple test runs, the influence of these special cases on the average thermal outcomes is small.

4.2. Vortex generation and melt plume dynamics

During descent (stage 1), a melt plume vortex forms in the wake behind the melting particle. The melt rises along the sides of the particle, forming circulating currents (vortex plumes) behind the particle as it travels downwards (insets of Fig. 4). Vortex formation in the wake of a fluid flow around spheres is well documented [15,31]. Hao and Tao observed that two circulating cells form in the wake of the flow around ice spheres, increasing heat transfer near the trailing edge [15]. Additionally, during droplet impact on a quiescent surface, vortices form at the leading edge of the droplet upon impact [22]. Similarly, rigid spheres falling in a liquid generate vortex rings downstream of the particle [30]. Contrary to rigid spheres, for melting ice particles, the vortex rings are formed not solely from the bath liquid, but also from the melting particle. The melt water appears to be originating from the upstream area (bottom) of the particle, and then recirculating towards the top of the particle. This observation indicates that the highest heat transfer rates (and hence melting rates) are indeed located near the leading edge of the particle due to forced convection. We also expect high heat transfer rates near the trailing edge due to the recirculating currents. This observation is consistent with findings of Hao and Tao [16], who show that local Nusselt numbers around a stationary spherical ice particle subject to laminar flow in a channel are highest at both the most upstream and downstream points of the particle.

Fig. 5 shows the typical long-term dynamics of the molten liquid for bath temperatures <50 °C after the initial penetration and plume vortex formation (stages 2,3). At these ltemperatures, where convective currents are negligible, the particles are approximately stationary after resurfacing. The particles maintain their positions after resurfacing until they have fully melted. During this process, a circular melt plume sinks and forms a vortex ring which spreads radially outwards from the particle, while traveling down in the reservoir due to the higher density of the cold ice melt. The melt continues to sink in single stream, expanding radially when hitting the bottom of the tank. Interestingly, throughout the entire melting process, the molten liquid follows the same path. A similar circular vortex ring was first documented by Thompson and Newall [25] in 1885 for droplet impact into liquid baths and has been studied since [23,24,26,32]. Rodriguez and Mesler [26] note the formation of a vortex ring when a droplet coalesces with the pool upon initial impact, instead of splashing. Interestingly, it was observed that vortex rings also form when a droplet coalesces without kinetic energy, *i.e.*, when gently placed onto the pool surface, indicating that surface tension is a driving mechanism in ring formation [32]. While the progression of a vortex ring has been described elsewhere, our observations of vortex rings from ice melt raise questions about the previously proposed explanations of its initial formation. Ray *et al.* [27] observed a crater formation upon droplet impact, where this crater eventually retracted to form

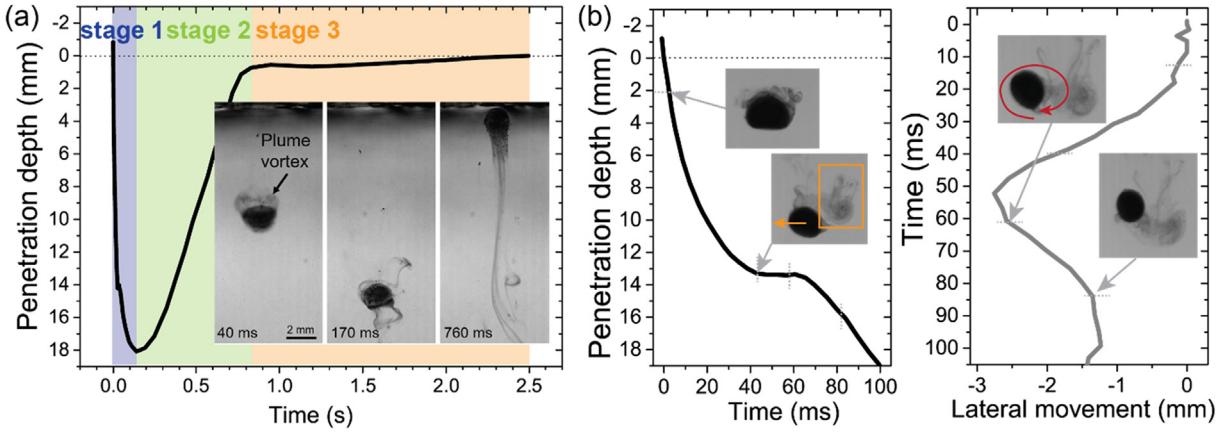

Fig. 4. (a) Diagram of penetration depth *vs.* time, highlighting the 3 stages of particle fluid and melting dynamics (T_{bath} = 50 °C, v = 1.5 m/s). Inset: Side-view images of ice particle impact with plume vortex formation and resurfacing. Ice particles are dyed with food color to visualize the mixing dynamics of the melt with the surrounding water. (b) Special case: Penetration depth and lateral movement of the ice particles at early times (stage 1), highlighting the influence of particle shape and rotation on penetration and melt dynamics (T_{bath} = 23 °C, v = 1.5 m/s).

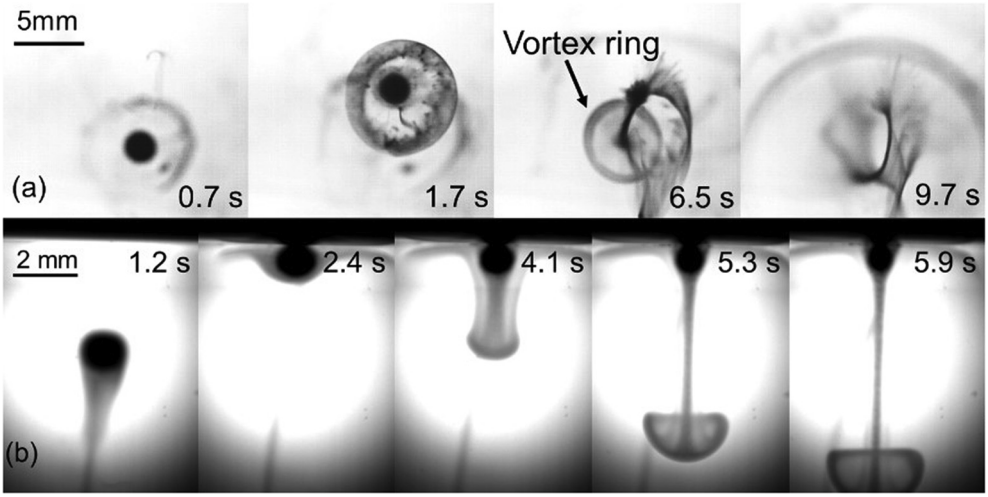

Fig. 5. Top-view (a) and side-view (b) images showing the temporal evolution of the melt plume and vortex formation (T_{bath} = 23 °C, v = 1.1 m/s).

the vortex ring. Rodrigues and Mesler [24], and later Lee *et al.* [33] proposed that upon impact capillary waves form between the leading edge of the droplet and the bath fluid, with fluid in the droplet circulating outwards it as enters the pool, creating a rotating volute and internal circulating currents within the impacting droplets. A crater expands behind the droplet and retracts. The volute motion forms a symmetrical vortex ring which expands as it travels downwards in the pool [27,34]. The ring decelerates during descent until reaching a maximum depth [23]. The vortex rings that we observe (see Fig. 5) are consistent with those previously described. However, our findings question the physical mechanism behind this vortex ring formation. We observe vortex ring formation after impact and resurfacing. While vortex plumes form during the first impact stage (see Fig. 4), they appear on the trailing edge of the particle. This is unlike the volutes that Rodrigues and Mesler [24,26] believe to drive ring formation. Additionally, the particles we use are solid, which eliminate the possibility of internal circulating currents during the initial stages of impact. Furthermore, the vortex ring observed in our experiments does not originate from the initial impact, but forms primarily after resurfacing and during melting. We propose instead that shear forces between the sinking colder (denser) melt and the warmer (less dense) fluids are the reason for this vortex ring formation, similar to those responsible for vortex ring generation during coalescence of two droplets on a bath surface [28] or sinking of an immiscible fluid in another [35]. As seen in Fig. 5b, we do not observe the later breakdown of the vortex ring due to Kelvin-Helmholtz instability, despite a Reynolds number $Re \approx 1$ [36].

At higher temperatures (>50 °C) we observe random ice particle motion during the melting process. After resurfacing (stage 3), the particle moves randomly across the surface of the bath, possibly due to some thermal convective currents (*e.g.*, Rayleigh-Bénard convection). Furthermore, at elevated temperatures the melt plume is irregularly shaped, as shown in Fig. 6. Even upon initial impact, the radially outflowing plume is not symmetrical and varies in shape between different experimental runs. Nonetheless, even with the movement of the ice particle, the melt still follows the same path and sinks to the bottom of the tank, where it spreads into a distorted oval shape.

From the observations from Figs. 5 and 6 we can identify two main phenomena which could have an important implication for additive manufacturing. First, Figs. 5 and 6 indicate that the molten liquid does not fully mix with the bath by the time it has melted. The melt water follows a distinct path and does not deviate from

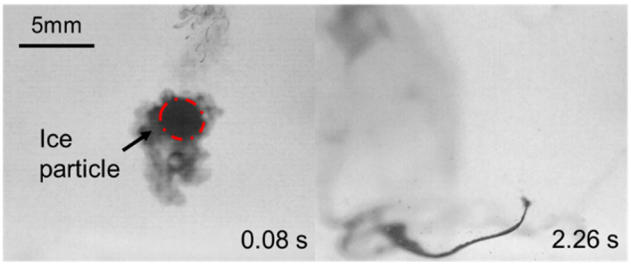

Fig. 6. Top-view images showing the irregular temporal evolution of the melt plume at elevated bath temperatures (T_{bath} = 70 °C, v = 1.1 m/s).

its initial trajectory. At high temperatures (>50 °C) the melt mixes to a greater degree than at lower bath temperatures. However, the melt plume still maintains a path and shape resembling a vortex ring that travels towards the bottom of the bath. In additive manufacturing, lack of mixing and thermal gradients can lead to inhomogeneous alloying and non-isotropic material properties [1,37]. Using Cu-based metallic glass powder deposited on a Zr-based glass substrate, Sun and Flores noted incomplete mixing of particles, as indicated by a compositional variation in the microstructure, resulting in a "mixed and unmixed melt zone" [38]. Correcting for this incomplete mixing in AM parts often requires additional processing, such as reglazing or other heat treatments, following the initial deposition [1]. Second, we observe that most of the melting happens after resurfacing. While one would be inclined to assume that, due to the negative buoyancy of solid metallic powder with respect to liquid metal, the here-studied model system with a positive buoyancy force of ice is not a good representation of actual DED systems, preliminary in-situ measurements obtained during deposition of titanium powder *via* the Laser Engineered Net Shaping (LENS) process reveal two types of particle dynamics: full penetration without resurfacing, or particle capture at the surface of the melt pool with subsequent melting. In the first case, melting times from our model system might not be representative, but cavity formation and bubble entrapment (see below) are to be expected in DED processes. In the second case, we expect melting dynamics to be similar. The latter case has also been recently reported by Volpp *et al.*, where surface tension or metal oxidation inhibit the power particle from penetrating the melt pool [39]. The particle remains floating and moving towards the center of the melt pool due to Marangoni convection before finally getting incorporated. We hypothesize that for floating par-

ticles melting is very similar to the here-reported phase change dynamics. Similarly, in case of dissimilar power and substrate materials, such as used during alloying, powder particles could have a lower density than the surrounding melt pool (for example, Ti powder in a steel pool), again likely resembling the behavior observed here.

4.3. Cavity generation and bubble entrapment

In addition to the melt plume and vortex formation, we also observe bubble formation trailing the particle at higher impact velocities ($v > 1.0$ m/s) during impact and initial decent (stage 1), as shown in Fig. 7. During impact, a funnel-shaped air cavity forms at the trailing (top) edge of the particle, similar to that documented by Akers and Belmonte for isothermal particle impact [19]. As the distance between particle and the equilibrium liquid-gas interface increases, this cavity pinches off, leading to an entrapped bubble at the trailing edge of the particle. While cavity formation and bubble entrapment have been studied extensively for isothermal particle impact [19,40,41], the existence of a cavity in the present experiments is at first surprising, given the low wetting angle of water on ice (static advancing contact angle $\theta_A = 11°$, as determined from a sessile droplet on an ice sheet). Previous studies revealed that cavity formation did not occur when smooth hydrophilic spheres impacted a liquid bath, but did form for impact of hydrophobic and textured spheres [30]. In the present experiments the ice spheres are inherently rough and porous [42], explaining the observed cavity formation. Aristoff *et al.* studied this cavity formation and found that at higher impact velocities, cavity formation and bubble entrapment were more consistent [21]. Cavity formation is divided into four regimes: quasi-static, shallow seal, deep seal, and surface seal [43,44]. With the impact velocities used in these experiments, we observe cavity formation in the quasi-static and shallow seal regimes. In the quasi static regime bubble entrapment is minimal and the cavity takes the shape of a static meniscus [43]. We see this type of cavity formation at velocities lower than 1.0 m/s. In the quasi-static regime the cavity collapses shortly after formation. In the shallow seal regime, bubble entrapment and deeper cavity formation is consistently observed [43]. The cavity pinches off later than quasi static cavity formation. We see this type of cavity formation at impact velocities greater than 1.0 m/s, as shown in Fig. 7. Speirs *et al.* further studied cavity formation, this time looking at various contact angles. In one experimental setup, coating spheres with Glaco was shown to influence cavity shape and formation [41]. In our experiments it is possible that Glaco residue from the petri dish adhered to some of the ice particles, resulting in inconsistent cavity formation. In additive manufacturing, this cavity formation and bubble entrapment can cause porosity in a solidified workpiece. While controlled porosity may be desirable in certain applications, such as biomedical implants where interconnected voids enable cell proliferation [45], porosity is more often a concern due to its negative effect on mechanical properties, particularly fatigue resistance [1,46].

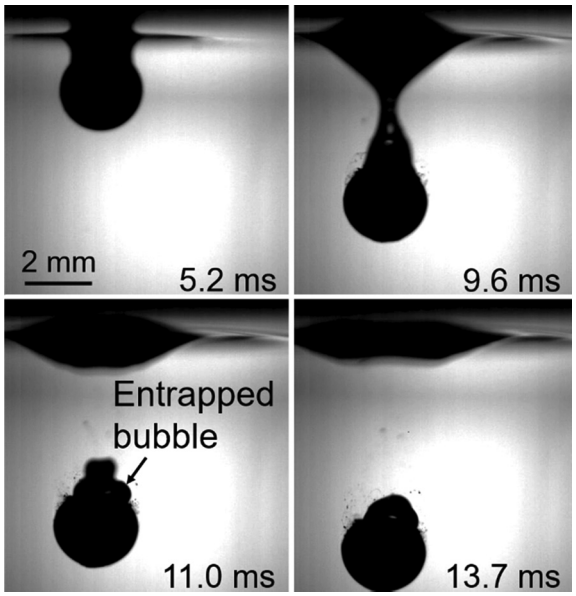

Fig. 7. Side-view snapshot of an ice particle impacting a bath at room temperature ($v = 1.8$ m/s), showing air cavity formation and bubble entrapment after snap-off.

4.4. Heat transfer

After the qualitative analysis of the impact and melt dynamics, we quantified melting times and heat transfer rates. Melt times were determined for each particle impact. Three experiments were conducted at each velocity-temperature combination. The averaged melt times are shown in Fig. 8. As expected, the particle melt time decreases as the bath temperature increases. With a 47 °C increase in bath temperature, the particle melt time decreases by around 7 s, from 9.7 s at 23 °C to 2.4 s at 70 °C for impact at 0.8 m/s.

In general, melt times decreased between the lowest and highest impact velocity. Interestingly, there is not a consistent decrease in melt time between each increase in velocity. We had expected that – with all other variables constant – the particle melt time would decrease with increasing velocity, since forced convection and consequently heat transfer during impact are also expected to increase [18,47]. Melissari and Argyropoulos [18] show a positive linear *Nu-Re* correlation for melting ice spheres in a flow channel. In our experiments, the bath temperature was kept consistent within a range of ±0.5 °C. Even though a 33 gauge needle was used to deposit all droplets prior to freezing, we did observe slight differences in frozen particle shape and size. We believe that these small variations had a greater influence on melt times than the variations in impact velocity. Error in volume calculations assuming a spherical particle shape ranged between 0.1 and 5.0%. This error is small enough that the spherical assumption is valid for the entire duration of the melt. However, over short time intervals, such as during the initial stage of impact, the error becomes significant for small changes in size. During impact, particle rotation was

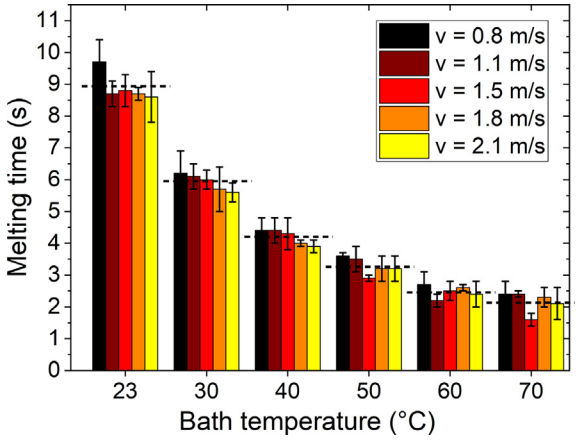

Fig. 8. Average melt times (in seconds) with the corresponding standard deviations from three impact trials for ice particles impacting heated water baths for different temperature-velocity combinations. Horizontal dashed lines represent the average melting times for all impact velocities at a given bath temperature.

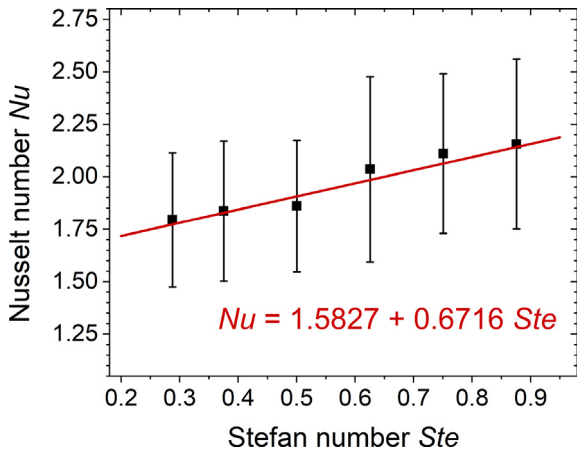

Fig. 9. Dependence of Nusselt number on Stefan number for ice particle impact into water baths of different temperatures with a linear regression. Error bars represent the standard deviation from 10 to 15 trials and the uncertainty associated with determining the equivalent particle diameter during melting (see Section 3 for a more detailed discussion on uncertainties).

observed. Particle rotation and asymmetry added additional uncertainty in our efforts to determine any unambiguous trend in melting times. Analysis of early melt times was inconclusive, and we were not able to determine a *Nu-Re* correlation for the early stages of impact. A more controlled environment would be needed to determine a correlation between impact velocity and heat transfer. Furthermore, as described in Section 4.2, most melting occurred after resurfacing, which inherently is independent of impact velocity.

To generalize our findings regarding the influence of bath temperature on melt times, we used dimensionless analysis. Following the analysis outlined in Section 3, we find that for spherical ice particles melting in a water bath (*i.e.*, after resurfacing), the Nusselt number varies linearly with the Stefan number, and lies between 1.7 and 2.2, as shown in Fig. 9. Using a linear regression, we find for quasi-spherical ice particles ($D \approx 2$ mm) and bath temperatures between 23 and 70 °C that:

$$Nu = 1.5827 + 0.6716Ste \quad (2)$$

We attribute the slight increase in Nusselt number, *i.e.*, heat transfer coefficient, with the Stefan number to enhanced natural convection around the melting particle at elevated temperatures. Interestingly, Nusselt numbers are slightly smaller than those expected for free convection around solid spheres submerged in water, for which $Nu = 2 + 0.5\,Ra^{1/4} \approx 5$–9 for 2 mm-diameter particles with our thermal conditions (with Rayleigh number *Ra*) [48]. We attribute this difference mainly to (1) the radius of the ice particle decreasing steadily as melting progresses, (2) the ice particle not being perfectly spherical, and (3) the ice particle not being fully submerged.

5. Conclusion and outlook

We reported the fluid and melting dynamics during ice particle impact on heated water baths. During impact, particles penetrate the bath surface, reach a maximum penetration depth, and resurface due to a positive buoyancy force of the ice with respect to liquid water. During impact we observe bubble entrapment, which in additive manufacturing could lead to unwanted porosity in the final workpiece. Furthermore, we observe the formation of plume vortices near the trailing edge of the particle during initial descent into the bath. After resurfacing we observe the downward propagation of larger vortex rings. A circular plume initially spreads radially outwards from the particle, along the bath surface. The plume then sinks downwards into the bath as it expands in radius. Melt water in the vortex ring emerges from a single melt path that remains distinct for the duration of the melt. While vortex rings have been previously documented for droplets, the proposed mechanisms driving their formation cannot explain the ring formation for melting ice we observed here. Instead, we propose that shear forces between the cold sinking melt and the hot bath water cause this vortex ring formation and propagation.

Melting times decrease with temperature, as expected, whereas the impact velocity does not have a unique influence on melt times or heat transfer, due to miniscule variations in particle size and bath temperature. However, we derive a positive linear correlation between Stefan and Nusselt numbers, *i.e.*, between bath temperature and heat transfer, where $Nu = 1.5827 + 0.6716\ Ste$. For high temperature applications like additive manufacturing, melting and mixing inconsistencies are expected to increase due to convective currents, such as Rayleigh-Bénard and Marangoni flow.

Our findings offer first insights into melting dynamics during particle impact into a heated bath or melt pool, which help explain some of the defects and inhomogeneities observed during direct energy deposition additive manufacturing. Future research should focus on baths with higher lateral temperature gradients, so that in addition to the possible occurrence of Rayleigh-Bénard convection, the effect of Marangoni convection on melting and mixing can be studied [10,49]. Synchronized high-speed optical and infrared imaging will be necessary to elucidate the effect of thermal gradients, currents, and particle pre-heating (*e.g.*, *via* the laser or electron beam, which could not only bring the particle to a higher temperature before impact, but also partially melt the particle or cause vertical temperature gradients within the particle) on melting dynamics. Furthermore, high-speed x-ray or neutron scattering measurements could shed light on the dynamics of metallic particles for the two impact scenarios during DED processing: Direct penetration without resurfacing, or floating and surface-melting, as discussed in Section 4.2. Findings in this work already indicate the importance of the interplay of buoyancy and convective currents (thermal or vortex-induced), which we expect to be of even higher importance for DED metallic additive manufacturing.

Declaration of Competing Interest

The authors declare that they have no known competing financial interests or personal relationships that could have appeared to influence the work reported in this paper.

Acknowledgements

PBW acknowledges the financial support from the McKelvey School of Engineering at Washington University in St. Louis. KB was partially supported through a Summer Undergraduate Research Award, sponsored by the Office of Undergraduate Research at Washington University in St. Louis. KMF's contribution to this work was partially supported by the National Science Foundation, Grant No. DMR-1809571.

References

[1] S.M. Thompson, L. Bian, N. Shamsaei, A. Yadollahi, An overview of Direct Laser Deposition for additive manufacturing; Part I: Transport phenomena, modeling and diagnostics, Addit. Manuf. 8 (2015) 36–62.
[2] D.D. Gu, W. Meiners, K. Wissenbach, R. Poprawe, Laser additive manufacturing of metallic components: materials, processes and mechanisms, Int. Mater. Rev. 57 (2012) 133–164, https://doi.org/10.1179/1743280411Y.0000000014.
[3] K. Shah, A.J. Pinkerton, A. Salman, L. Li, Effects of melt pool variables and process parameters in laser direct metal deposition of aerospace alloys, Mater. Manuf. Process. 25 (2010) 1372–1380, https://doi.org/10.1080/10426914.2010.480999.

[4] V.V. Semak, J.A. Hopkins, M.H. McCay, T.D. McCay, Melt pool dynamics during laser welding, J. Phys. Appl. Phys. 28 (1995) 2443–2450, https://doi.org/10.1088/0022-3727/28/12/008.
[5] T. Scharowsky, F. Osmanlic, R.F. Singer, C. Körner, Melt pool dynamics during selective electron beam melting, Appl. Phys. A 114 (2014) 1303–1307, https://doi.org/10.1007/s00339-013-7944-4.
[6] W.J. Sames, F.A. List, S. Pannala, R.R. Dehoff, S.S. Babu, The metallurgy and processing science of metal additive manufacturing, Int. Mater. Rev. 61 (2016) 315–360, https://doi.org/10.1080/09506608.2015.1116649.
[7] K. Bartkowiak, Direct laser deposition process within spectrographic analysis in situ, Phys. Procedia 5 (2010) 623–629, https://doi.org/10.1016/j.phpro.2010.08.090.
[8] P. Berger, H. Hügel, T. Graf, Understanding pore formation in laser beam welding, Phys. Procedia 12 (2011) 241–247, https://doi.org/10.1016/j.phpro.2011.03.031.
[9] V. Manvatkar, A. De, T. DebRoy, Spatial variation of melt pool geometry, peak temperature and solidification parameters during laser assisted additive manufacturing process, Mater. Sci. Technol. 31 (2015) 924–930, https://doi.org/10.1179/1743284714Y.0000000701.
[10] X. He, J. Mazumder, Transport phenomena during direct metal deposition, J. Appl. Phys. 101 (2007), https://doi.org/10.1063/1.2710780 053113.
[11] O.B. Kovalev, I.O. Kovaleva, I.Yu. Smurov, Numerical investigation of gas-disperse jet flows created by coaxial nozzles during the laser direct material deposition, J. Mater. Process. Technol. 249 (2017) 118–127, https://doi.org/10.1016/j.jmatprotec.2017.05.041.
[12] I. Smurov, M. Doubenskaia, S. Grigoriev, A. Nazarov, Optical monitoring in laser cladding of Ti6Al4V, J. Therm. Spray Technol. 21 (2012) 1357–1362, https://doi.org/10.1007/s11666-012-9808-4.
[13] Z. Li, K. Mukai, M. Zeze, K.C. Mills, Determination of the surface tension of liquid stainless steel, J. Mater. Sci. 40 (2005) 2191–2195, https://doi.org/10.1007/s10853-005-1931-x.
[14] M. Korolczuk-Hejnak, P. Migas, Analysis of selected liquid steel viscosity/Analiza Lepkosci Wybranych Gatunków Stali W Stanie Ciekłym, Arch. Metall. Mater. 57 (2012), https://doi.org/10.2478/v10172-012-0107-3.
[15] Y.L. Hao, Y.-X. Tao, Melting of a solid sphere under forced and mixed convection: flow characteristics, J. Heat Transf. 123 (2001) 937, https://doi.org/10.1115/1.1389466.
[16] Y. Hao, Y.-X. Tao, Heat transfer characteristics of melting ice spheres under forced and mixed convection, J. Heat Transf. 124 (2002) 891–903.
[17] A. Kumar, S. Roy, Heat transfer characteristics during melting of a metal spherical particle in its own liquid, Int. J. Therm. Sci. 49 (2010) 397–408.
[18] B. Melissari, S.A. Argyropoulos, Measurement of magnitude and direction of velocity in high-temperature liquid metals. Part I: Mathematical modeling, Metall. Mater. Trans. B. 36 (2005) 691–700, https://doi.org/10.1007/s11663-005-0060-x.
[19] B. Akers, A. Belmonte, Impact dynamics of a solid sphere falling into a viscoelastic micellar fluid, J. Non-Newton. Fluid Mech. 135 (2006) 97–108, https://doi.org/10.1016/j.jnnfm.2006.01.004.
[20] J.O. Marston, I.U. Vakarelski, S.T. Thoroddsen, Bubble entrapment during sphere impact onto quiescent liquid surfaces, J. Fluid Mech. 680 (2011) 660–670, https://doi.org/10.1017/jfm.2011.202.
[21] J.M. Aristoff, T.T. Truscott, A.H. Techet, J.W.M. Bush, The water entry of decelerating spheres, Phys. Fluids 22 (2010), https://doi.org/10.1063/1.3309454 032102.
[22] G. Agbaglah, M.-J. Thoraval, S.T. Thoroddsen, L.V. Zhang, K. Fezzaa, R.D. Deegan, Drop impact into a deep pool: vortex shedding and jet formation, J. Fluid Mech. 764 (2015) R1, https://doi.org/10.1017/jfm.2014.723.
[23] P.N. Shankar, M. Kumar, Vortex rings generated by drops just coalescing with a pool, Phys. Fluids 7 (1995) 737–746, https://doi.org/10.1063/1.868597.
[24] F. Rodriguez, R. Mesler, The penetration of drop-formed vortex rings into pools of liquid, J. Colloid Interface Sci. 121 (1988) 121–129, https://doi.org/10.1016/0021-9797(88)90414-6.
[25] J.J. Thomson, H.F. Newall, On the formation of vortex rings by drops falling into liquids, and some allied phenomena, Proc. R. Soc. Lond. 39 (1886) 417–436.
[26] F. Rodriguez, R. Mesler, Some drops don't splash, J. Colloid Interface Sci. 106 (1985) 347–352, https://doi.org/10.1016/S0021-9797(85)80008-4.
[27] B. Ray, G. Biswas, A. Sharma, Vortex ring formation on drop coalescence with underlying liquid, in: Vol. 3 Gas Turbine Heat Transf. Transp. Phenom. Mater. Process. Manuf. Heat Transf. Electron. Equip. Symp. Honor Profr. Richard Goldstein Symp. Honor Prof Spalding Symp. Honor Prof Arthur E Bergles, ASME, Minneapolis, Minnesota, USA, 2013: p. V003T21A012. doi: 10.1115/HT2013-17711.
[28] C. Ortiz-Dueñas, J. Kim, E.K. Longmire, Investigation of liquid–liquid drop coalescence using tomographic PIV, Exp. Fluids 49 (2010) 111–129, https://doi.org/10.1007/s00348-009-0810-7.
[29] S. Al Issa, P. Weisensee, R. Macián-Juan, Experimental investigation of steam bubble condensation in vertical large diameter geometry under atmospheric pressure and different flow conditions, Int. J. Heat Mass Transf. 70 (2014) 918–929, https://doi.org/10.1016/j.ijheatmasstransfer.2013.11.049.
[30] T.T. Truscott, B.P. Epps, A.H. Techet, Unsteady forces on spheres during free-surface water entry, J. Fluid Mech. 704 (2012) 173–210.
[31] H. Sakamoto, H. Haniu, A study on vortex shedding from spheres in a uniform flow, J. Fluids Eng. 112 (1990) 386–392.
[32] K. Shariff, A. Leonard, Vortex rings, Annu. Rev. Fluid Mech. 24 (1992) 235–279.
[33] J.S. Lee, S.J. Park, J.H. Lee, B.M. Weon, K. Fezzaa, J.H. Je, Origin and dynamics of vortex rings in drop splashing, Nat. Commun. 6 (2015) 8187, https://doi.org/10.1038/ncomms9187.
[34] A. Tinaikar, S. Advaith, S. Basu, Understanding evolution of vortex rings in viscous fluids, J. Fluid Mech. 836 (2018) 873–909, https://doi.org/10.1017/jfm.2017.815.
[35] N. Baumann, D.D. Joseph, P. Mohr, Y. Renardy, Vortex rings of one fluid in another in free fall, Phys. Fluids Fluid Dyn. 4 (1992) 567–580, https://doi.org/10.1063/1.858328.
[36] M.C. Rogers, S.W. Morris, Natural versus forced convection in laminar starting plumes, Phys. Fluids 21 (2009), https://doi.org/10.1063/1.3207837 083601.
[37] L. Bian, S. Thompson, N. Shamsaei, Mechanical properties and microstructural features of direct laser-deposited Ti-6Al-4V, 2015. doi: 10.1007/s11837-015-1308-9.
[38] H. Sun, K.M. Flores, Laser deposition of a Cu-based metallic glass powder on a Zr-based glass substrate, J. Mater. Res. 23 (2008) 2692–2703, https://doi.org/10.1557/JMR.2008.0329.
[39] J. Volpp, Behavior of powder particles on melt pool surfaces, Int. J. Adv. Manuf. Technol. 102 (2019) 2201–2210, https://doi.org/10.1007/s00170-018-03261-1.
[40] D. Li, J. Zhang, M. Zhang, B. Huang, X. Ma, G. Wang, Experimental study on water entry of spheres with different surface wettability, Ocean Eng. 187 (2019), https://doi.org/10.1016/j.oceaneng.2019.106123 106123.
[41] N. Speirs, M. Mansoor, J. Belden, T. Truscott, Water entry of spheres with various contact angles, J. Fluid Mech. 862 (2019), https://doi.org/10.1017/jfm.2018.985.
[42] F. Chu, X. Zhang, S. Li, H. Jin, J. Zhang, X. Wu, D. Wen, Bubble formation in freezing droplets, Phys. Rev. Fluids 4 (2019), https://doi.org/10.1103/PhysRevFluids. 4.071601 071601.
[43] J.M. Aristoff, J.W.M. Bush, Water entry of small hydrophobic spheres, J. Fluid Mech. 619 (2009) 45–78, https://doi.org/10.1017/S0022112008004382.
[44] T. Truscott, B. Epps, J. Belden, Water entry of projectiles, Annu. Rev. Fluid Mech. 46 (2013), https://doi.org/10.1146/annurev-fluid-011212-140753.
[45] R. M. Mahamood, E. Akinlabi, D.M. Shukla, S. Pityana, Characterizing the effect of processing parameters on the porosity of laser deposited titanium alloy powder, in: Proc. Int. MultiConference Eng. Comput. Sci. 2014 Vol II IMECS 2014, Hong Kong, 2014.
[46] G.K.L. Ng, A.E.W. Jarfors, G. Bi, H.Y. Zheng, Porosity formation and gas bubble retention in laser metal deposition, Appl. Phys. A 97 (2009) 641–649, https://doi.org/10.1007/s00339-009-5266-3.
[47] H. Kramers, Heat transfer from spheres to flowing media, Physica 12 (1946) 61–80.
[48] W.S. Amato, T. Chi, Free convection heat transfer from isothermal spheres in water, Int. J. Heat Mass Transf. 15 (1972) 327–339, https://doi.org/10.1016/0017-9310(72)90078-6.
[49] P.S. Wei, H.J. Liu, C.L. Lin, Scaling weld or melt pool shape induced by thermocapillary convection, Int. J. Heat Mass Transf. 55 (2012) 2328–2337, https://doi.org/10.1016/j.ijheatmasstransfer.2012.01.034.